

Measuring the Coulomb time shift in high-order harmonic generation

Shengjun Yue(岳生俊), Siqi Song(宋思琦), Ruofeng Zhong(钟若峰), Jiangkun Li(李江坤), Haiyuan Yu(于海元), and Hongchuan Du(杜洪川)

Citation: Chin. Phys. B, 2026, 35 (**4**): 043201. DOI: 10.1088/1674-1056/ae1951
http://cpb.iphy.ac.cn; http://iopscience.iop.org/cpb

What follows is a list of articles you may be interested in

Comparison of high-order harmonic generation in defect-free and defective solids with different time delays

Shujie Zhao(赵书杰), Yuanzuo Li(李源作), Jun Zhang(张军), and Xuefei Pan(潘雪飞)
Chin. Phys. B, 2025, 34 (**12**): 123201. DOI: 10.1088/1674-1056/addd82

Influence of excited states in high-order harmonic generation at intense mid-infrared field

Yan Fang(方言), Da-Wei Tian(田大纬), Yue Cao(曹玥), Xiao-Lei Hao(郝小雷), and Zheng Shu(舒正)
Chin. Phys. B, 2025, 34 (**10**): 103201. DOI: 10.1088/1674-1056/adda0d

High-order harmonic generation of methane in an elliptically polarized field

Shu-Shan Zhou(周书山), Yu-Long Li(李玉龙), Zhi-Xue Zhao(赵志学), Man Xing(幸满), Nan Xu(许楠), Hao Wang(王浩), Jun Wang(王俊), Xi Zhao(赵曦), and Mu-Hong Hu(胡木宏)
Chin. Phys. B, 2025, 34 (**6**): 063202. DOI: 10.1088/1674-1056/adcb9d

Frequency shifts of high-order harmonics from ZnO crystals by chirped laser pulses

Yu Zhao(赵宇), Xiao-Jin Liu(刘晓瑾), Shuang Wang(王爽), Xiao-Xin Huo(霍晓鑫), Yun-He Xing(邢云鹤), and Jun Zhang(张军)
Chin. Phys. B, 2025, 34 (**3**): 033201. DOI: 10.1088/1674-1056/ada9dc

Interference of harmonics emitted by different tunneling momentum channels in laser fields

Ling-Yu Zhang(张玲玉), Zhuo-Xuan Xie(谢卓璇), Can Wang(王灿), Xin-Lei Ge(葛鑫磊), and Jing Guo(郭静)
Chin. Phys. B, 2024, 33 (**9**): 093201. DOI: 10.1088/1674-1056/ad5d95

TOPICAL REVIEW — Ultrafast physics in atomic, molecular and optical systems

Measuring the Coulomb time shift in high-order harmonic generation

Shengjun Yue(岳生俊)[1], Siqi Song(宋思琦)[1], Ruofeng Zhong(钟若峰)[1], Jiangkun Li(李江坤)[1,2], Haiyuan Yu(于海元)[1,†], and Hongchuan Du(杜洪川)[1,‡]

[1] *School of Nuclear Science and Technology, Lanzhou University, Lanzhou* 730000, *China*
[2] *Airborne Survey and Remote Sensing Center of Nuclear Industry, Shijiazhuang* 050002, *China*

(Received 16 August 2025; revised manuscript received 28 October 2025; accepted manuscript online 30 October 2025)

High-order harmonic generation (HHG), a key nonlinear phenomenon in strong-field physics, enables ultrafast detection on the attosecond timescale. Quantifying ionization/recombination times is essential for trajectory-resolved high-harmonic spectroscopy and for benchmarking its temporal resolution. In this review, we summarize our recent studies [*Phys. Rev. A* **105** L041103 (2022), *Phys. Rev. A* **106** 023117 (2022), *Phys. Rev. A* **107** 063102 (2023), *Phys. Rev. A* **111** 039902 (2025)] on the role of electron–core interactions in HHG. Employing the classical trajectory model, analytical R-matrix theory, and numerical solutions of time-dependent Schrödinger equations for helium, we reveal how Coulomb attraction induces subtle shifts in ionization and recombination times. Such effects emerge as observable signatures under orthogonally polarized bichromatic fields at high probe frequencies. Because of the direct experimental relevance of these findings, this review seeks to stimulate further experimental efforts to control and resolve electron dynamics in HHG. In the future, it will be of great interest to (i) refine retrieval methods by incorporating Coulomb corrections beyond the static-field approximation, and (ii) advance two-color detection techniques with the capability to reconstruct complete quantum trajectories in HHG.

Keywords: high-order harmonic generation, ultrafast electron dynamics, Coulomb effects, attosecond science

PACS: 32.80.Qk, 42.65.Ky, 42.65.–k, 42.65.Re

DOI: 10.1088/1674-1056/ae1951 **CSTR:** 32038.14.CPB.ae1951

1. Introduction

Physicists contemplate how the world operates, and this curiosity serves as the primary driving force behind the field of physics. At the heart of this understanding is the motion of matter, a fundamental principle essential to grasping the dynamics of the Universe. After Harold Eugene Edgerton captured a fleeting moment of a bullet piercing an apple, advanced imaging techniques have allowed researchers to pinpoint movement on the scale of picometers and to capture action that happens in femtoseconds.[1–4] However, achieving ultrafast detection with attosecond or even zeptosecond time resolution still requires indirect observation methods. Thanks to breakthroughs in laser technology and strong-field physics, ultrafast science has now opened the door to the attosecond realm.[5]

The measurement and resolution of ultrafast quantum dynamics depend on physical observables. In strong-field physics, two primary observables are commonly used: the photoelectron momentum distribution (PMD) and high-order harmonic generation (HHG).[6–11] PMD provides direct electron momentum detection, yielding strictly real-valued measurements. In contrast, HHG does not involve direct electron detection. Instead, it captures high-frequency photons emitted during electron recombination into the ground state. This indirect nature makes high-harmonic spectroscopy (HHS) particularly valuable for probing the quantum characteristics of matter because it uniquely reflects the complex structure of the electronic wavefunction.

The HHG dynamics are well captured by the classical three-step process,[12] which consists of ionization, acceleration, and recombination. The electron's motion during acceleration exhibits quasi-classical behavior, permitting trajectory-based descriptions. Each HHG trajectory is characterized by three parameters: ionization times, recombination times, and the returning electron's kinetic energy. However, within the quantum-mechanical framework, the strong-field approximation (SFA)[13] and the quantum-orbit (QO) model[14] reveal that both ionization and recombination times must be treated as complex quantities. Although HHS successfully probes various ultrafast phenomena, including nonadiabatic tunneling dynamics,[15,16] Auger decay,[17,18] nuclear vibrations in molecules,[19–21] and picometer-scale imaging of valence electrons in solids,[22] accurate measurement of ionization and return times is essential for trajectory-resolved HHS.

Two prevalent experimental strategies have been developed to access the ionization and recombination times in HHG by manipulating tailored laser-field configurations. One approach, often referred to as the phase-gate technique, ex-

†Corresponding author. E-mail: yuhy22@lzu.edu.cn
‡Corresponding author. E-mail: duhch@lzu.edu.cn

© 2026 Chinese Physical Society and IOP Publishing Ltd. All rights, including for text and data mining, AI training, and similar technologies, are reserved.

tracts the emission time from the variation of even-order harmonics with respect to the phase delay between two parallel color components.[23] Another widely used method, known as the displacement/velocity gate scheme, utilizes orthogonally polarized two-color (OTC) laser pulses to determine the real parts of the ionization and recombination times associated with short electron trajectories.[24,25] In these pioneering schemes, the extracted time information shows good agreement with Coulomb-free quantum-orbital predictions. Nevertheless, the Coulomb attraction between the departing electron and the parent ion inevitably slows the electron's motion, necessitating compensations in the retrieved time information.

In this concise overview, we revisit our recent investigations,[26–29] where numerical simulations based on the time-dependent Schrödinger equation (TDSE) were employed to explore how the Coulomb potential influences time shifts in HHG within an OTC field. Our findings reveal that operating at higher streaking frequencies provides a distinct benefit: the Coulomb-corrected ionization times can be reliably extracted through a direct analysis, without explicitly embedding Coulomb terms into the retrieval algorithm. Conversely, when a conventional ω–2ω configuration incorporating a 400 nm streaking field is used, such corrections become indispensable for uncovering the associated time shifts. These insights highlight the importance of field configuration and frequency in accurately accessing attosecond ionization dynamics and pave the way for future studies aiming to disentangle Coulomb effects in strong-field processes.

2. Theoretical methods

2.1. Time-dependent Schrödinger equation

The interaction between strong laser fields and helium atoms is described by the TDSE within the single-active-electron approximation. In the length gauge, the two-dimensional TDSE is given by

$$\mathrm{i}\frac{\partial}{\partial t}\psi(\boldsymbol{r},t)=\left(-\frac{\nabla_{\boldsymbol{r}}^2}{2}+V(\boldsymbol{r})+\boldsymbol{r}\cdot\boldsymbol{E}(t)\right)\psi(\boldsymbol{r},t). \tag{1}$$

Here, Hartree atomic units are implemented consistently unless noted otherwise. The model employs a soft-core potential of $V(\boldsymbol{r})=-1/\sqrt{\boldsymbol{r}^2+0.0684}$, which reproduces the ionization potential of helium, $I_\mathrm{p}=0.9$ a.u. The OTC laser field $\boldsymbol{E}(t)=-\dot{\boldsymbol{A}}(t)$ is defined through the vector potential

$$\boldsymbol{A}(t)=-\frac{E_0}{\omega}f(t)\left[\sin(\omega t)\hat{\boldsymbol{e}}_x+\frac{\varepsilon}{n}\sin(n\omega t+\phi)\hat{\boldsymbol{e}}_y\right], \tag{2}$$

where $\hat{\boldsymbol{e}}_x$ and $\hat{\boldsymbol{e}}_y$ denote Cartesian unit vectors. Here, E_0 and ω correspond, respectively, to peak amplitude and angular frequency of an 800 nm fundamental pulse (4.0×10^{14} W/cm^2 intensity). The relative phase ϕ, termed the two-color phase delay, controls the phase offset between the fundamental and streaking fields, while $n\in\mathbb{R}^+$ sets the streaking frequency to $n\omega$. Our numerical implementation employs a trapezoidal temporal envelope $f(t)$ spanning $-T$ to $2T$ ($T=2\pi/\omega$) with single-cycle ramps. To suppress HHG contributions from the pulse boundaries, the rising edge follows $\cos^6(\omega t/4)$, while the falling edge obeys $\sin^6(\omega t/4)$. The streaking field relative amplitude is fixed at $\varepsilon=0.02$.

We numerically solve the TDSE via the Crank–Nicolson method[30,31] using a temporal resolution of $\Delta t=0.05$ a.u. The simulation box has a size of $L_x\times L_y=280\times100$ a.u., discretized into 2800×1000 grid points. To prevent reflections at the boundaries, the wave-function is multiplied at each time step by mask functions. The mask function along the x axis is defined as $F(x)=\cos^{1/8}\left[\pi\left(|x|-x_0\right)/\left(L_x-2x_0\right)\right]$ for $|x|\geq x_0$ and $F(x)=1$ for $|x|\leq x_0$, where $x_0=7L_x/18$. A similar approach is applied in the y direction, where y_0 is set to $7L_y/18$. Following wavefunction propagation, Cartesian components of the dipole acceleration $\boldsymbol{a}(t)=(a_x(t),a_y(t))$ are computed through Ehrenfest's theorem[32]

$$\boldsymbol{a}(t)=\left\langle\psi(\boldsymbol{r},t)\middle|\nabla_{\boldsymbol{r}}\left[V(\boldsymbol{r})+\boldsymbol{r}\cdot\boldsymbol{E}(t)\right]\middle|\psi(\boldsymbol{r},t)\right\rangle. \tag{3}$$

2.2. Gabor transform

The harmonic spectrum is presented in Fig. 1, in which the wavelength of the fundamental field (probe field) is 800 nm (400 nm). The x-polarized (red) and y-polarized (blue) harmonic components demonstrate a significant intensity contrast as a result of the weak amplitude of the streaking field. Both spectra display plateau regions from harmonics 20 to 65, ending near the theoretical cutoff energy $E_\mathrm{c}=I_\mathrm{p}+3.17U_\mathrm{p}$, where $U_\mathrm{p}=E_0^2/\left(4\omega^2\right)$ is the ponderomotive energy. However, one of the main challenges in numerical simulations of HHG lies in the fact that the harmonic spectrum alone does not directly reveal the ionization and recombination times. This ambiguity stems from multiple quantum trajectories contributing to one single harmonic order. While experiments separate long/short trajectories via phase-matching adjustments, our single-atom analysis employs Gabor time-frequency transformation[25,33,34]

$$\begin{aligned}I_\mathrm{G}(\Omega,t)&=\sum_{j=x,y}\left|\int\mathrm{d}t' a_j(t')\,\mathrm{e}^{-\frac{(t'-t)^2}{2\sigma^2}+\mathrm{i}\Omega t'}\right|^2\\&=I_{\mathrm{G}x}(\Omega,t)+I_{\mathrm{G}y}(\Omega,t),\end{aligned} \tag{4}$$

with $\sigma=\frac{1}{3\omega}$ and $a_j(t')$ being the jth component ($j=x,y$) of the dipole acceleration. For each Ω, we extract the maxima $I_\mathrm{G}(\Omega,t_\mathrm{e})$ in specific temporal windows: $t\in[0.3T,0.7T]$ (short trajectory) and $t\in[0.7T,1.0T]$ (long trajectory), as illustrated in Fig. 2. The corresponding times t_e define two ϕ-dependent observables: the harmonic intensity $I_\mathrm{G}(\Omega,t_\mathrm{e})$ and the amplitude ratio $R=\sqrt{I_{\mathrm{G}y}(\Omega,t_\mathrm{e})/I_{\mathrm{G}x}(\Omega,t_\mathrm{e})}$, forming the basis for time-retrieval methodology.

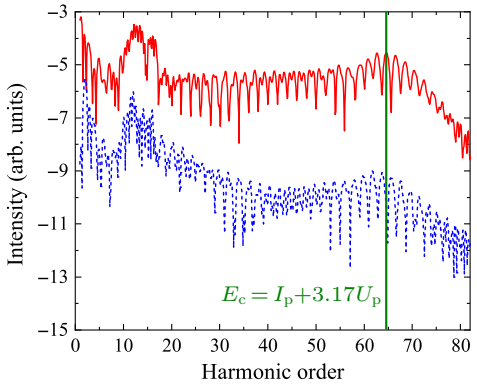


Fig. 1. The harmonic spectra of He driven by an ω–2ω laser field ($\omega = 0.057$ a.u., $E_0 = 0.1068$ a.u., $\phi = 0$) are shown for components polarized along the x axis (red curves) and the y axis (blue curves). Adapted from Refs. [28,29].

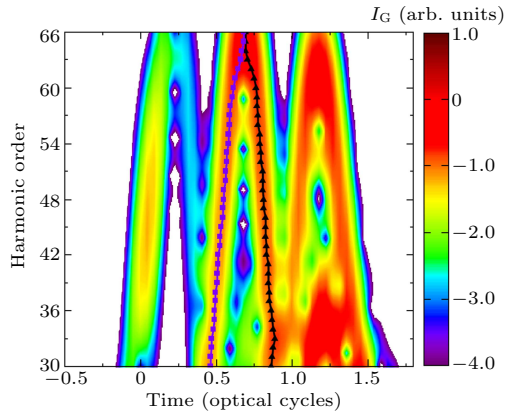


Fig. 2. Gabor analysis of HHG driven by ω–2ω fields at zero phase delay ($\phi = 0$). The fundamental 800 nm laser pulse has an intensity of 4.0×10^{14} W/cm^2. Purple-connected squares (black-connected triangles) map peak loci of Gabor distribution corresponding to short (long) quantum paths. Adapted from Ref. [27].

2.3. Two-color gate

Within the TDSE framework, time is treated as a parameter rather than an experimentally measurable quantity, unlike PMD or HHS. Therefore, establishing a connection between time-related quantities and observable signals is essential for retrieving temporal information from experimental data. Under weak probe conditions (here $\varepsilon = 0.02$), the fundamental field primarily dictates the ionization (t_i) and recombination times (t_r). The influence of the weak field on the experimental observables can be quantitatively analyzed, as previously described in Refs. [24,25].

For recollision in HHG via Coulomb-free trajectories, the electron must return to its parent ion, which means zero transverse displacement $y(t_r) - y(t_i) = 0$. This gate condition determines the required initial transverse velocity

$$v_{y0} = -\frac{\varepsilon E_0}{n\omega}\left[\sin(\varphi_i) + \frac{\cos(\varphi_r) - \cos(\varphi_i)}{n\omega(t_r - t_i)}\right], \tag{5}$$

where $\varphi_i = n\omega t_i + \phi$ and $\varphi_r = n\omega t_r + \phi$. As established in Refs. [35,36], the maximum harmonic intensity means $v_{y0} = 0$. Therefore, Eq. (5) constrains (t_i, t_r) at the yield-maximizing phase $\bar{\phi}_1$, a condition commonly known as the displacement gate.

For harmonics with linear polarization, the amplitude ratio R corresponds to the polarization angle θ via $R = \tan\theta$. Experimental measurements in Ref. [24] determined R as the amplitude ratio between even and odd consecutive harmonics. This measurement is feasible because, for a ω–2ω OTC field, the harmonic field in the y direction is $T/2$-periodic in time, whereas the harmonic field in the x direction undergoes a sign reversal between consecutive half-cycles of the fundamental field. Fourier transformation thus yields even harmonics polarized along the y-axis and odd harmonics along the x-axis.[24,37] If the ground state exhibits spherical symmetry, the harmonic polarization angle matches the electron return angle,[37] allowing R to be written as $\left|v_y(t_r)/v_x(t_r)\right|$. Here, $v_y(t_r)$ is computed from Coulomb-free trajectories, while $v_x(t_r) = \sqrt{2(\Omega - I_p)}$.

Finally, we have the following expression for R

$$R = \frac{\varepsilon E_0/(n\omega)}{\sqrt{2(\Omega - I_p)}}\left|\sin(\varphi_r) + \frac{\cos(\varphi_r) - \cos(\varphi_i)}{n\omega(t_r - t_i)}\right|. \tag{6}$$

By maximizing R through two-color delay optimization, Eq. (6) constrains time information (t_i, t_r) via the velocity gate mechanism.

Experimental results or TDSE computations yield optimal phase values: $\bar{\phi}_1$ maximizes harmonic intensity, while $\bar{\phi}_2$ maximizes the amplitude ratio R. These two optimal phases enable the determination of ionization and return times (t_i, t_r) through displacement and velocity gate constraints. In the QO framework,[25] we incorporate complex time variables into Eqs. (5) and (6), resulting in the dual retrieval conditions:

$$\mathrm{Re}\, v_{y0} = 0, \tag{7}$$

$$\partial R/\partial\phi = 0. \tag{8}$$

3. Coulomb-induced ionization time shift for short trajectories

In this section, we present the frequency-dependent behavior of two-color HHS for probing ionization times on the attosecond timescale, focusing on short quantum trajectories.[26] The two observables used for analysis are presented in Fig. 3: TDSE-computed harmonic intensity (left) and amplitude ratio (right) for laser pulses ω–2ω (top) and ω–4.3ω (bottom). Optimized phases maximizing these observables per harmonic order are marked by orange lines. The white curves depict the corresponding SFA-calculated phases using the intensity expression

$$I_s(\Omega) = \left|\exp\left(i\left(\Omega t_r - S_v\right)\right)\right|^2, \tag{9}$$

with quasi-classical action

$$S_v = \int_{t_i}^{t_r} \mathrm{d}t\left(v^2(t)/2 + I_p\right). \tag{10}$$

Here, the electron velocity $\boldsymbol{v}(t) \equiv \boldsymbol{p}(t_\mathrm{i}, t_\mathrm{r}) + \boldsymbol{A}(t)$ employs saddle-point momentum

$$\boldsymbol{p}(t_\mathrm{i}, t_\mathrm{r}) = -\frac{1}{t_\mathrm{r} - t_\mathrm{i}} \int_{t_\mathrm{i}}^{t_\mathrm{r}} \boldsymbol{A}(t)\,\mathrm{d}t. \tag{11}$$

The complex times $t_\mathrm{i} = t_\mathrm{i}^0 + \mathrm{i}\,\mathrm{Im}\,t_\mathrm{i}$ and $t_\mathrm{r} = t_\mathrm{r}^0 + \mathrm{i}\,\mathrm{Im}\,t_\mathrm{r}$ satisfy the saddle-point equations derived from the QO model[14]

$$\frac{\boldsymbol{v}^2(t_\mathrm{i})}{2} = -I_\mathrm{p}, \quad \frac{\boldsymbol{v}^2(t_\mathrm{r})}{2} = \Omega - I_\mathrm{p}. \tag{12}$$

Under weak-field conditions, the y-component of the vector potential $\boldsymbol{A}(t)$ is omitted from Eq. (12) unless explicitly noted.

In the ω–2ω case, the optimal phases obtained from the TDSE simulations show excellent agreement with those predicted by the SFA [Figs. 3(a) and 4(b)], despite the exclusion of Coulomb interactions. This confirms the earlier findings.[25] When considering the case of ω–4.3ω, the optimal phase $\bar{\phi}_2$ remains in good agreement between SFA and TDSE results [Fig. 3(d)]. In contrast, a measurable divergence emerges in the harmonic intensity phases ($\bar{\phi}_1$) [Fig. 3(c)]. This phase shift is attributed to Coulomb effects, which provides insight into the Coulomb-induced shift in the ionization time.

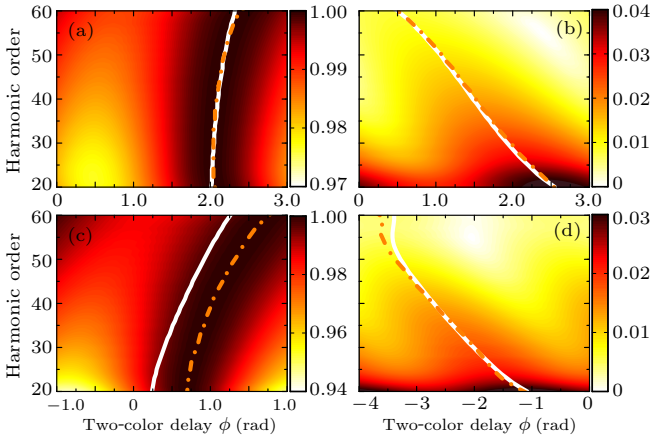


Fig. 3. Pseudocolor maps show numerical results as functions of harmonic order (q) and two-color phase offset. (a), (c) Normalized HHG spectral intensity; (b), (d) polarization ratio $R = |v_y(t_\mathrm{r})/v_x(t_\mathrm{r})|$. Top: 2ω streaking field. Bottom: 4.3ω streaking field. Optimization extrema are indicated by the white solid line (SFA) and the orange dashed-dotted line (TDSE). Taken from Ref. [26].

Before analyzing the ionization time shift in the ω–$n\omega$ configuration, we introduce two key assumptions that significantly simplify the analysis. First, ionization times are determined exclusively from the harmonic intensity using the known QO recombination times. Our numerical tests confirm that this assumption introduces a negligible error in the extracted ionization times. This aligns with the results of the analytical R-matrix (ARM) model,[38] which demonstrates a weaker Coulomb sensitivity for recombination times than for ionization times. This is further supported by minimal Coulomb focusing effects on polarization angles for short trajectories.[39] In addition, the imaginary part of t_r is set to zero.[25,30] Second, we define the imaginary part $\mathrm{Im}\,t_\mathrm{i}$ by Keldysh time, given by $\mathrm{Im}\,t_\mathrm{i} = \sqrt{2I_\mathrm{p}}/|E_x(t_\mathrm{i}^0)|$.[41] Through TDSE-derived optimal phases $\bar{\phi}_1$, t_i^0 can then be retrieved using Eqs (5) and (7).

Figure 4(a) displays the retrieved ionization time at multiple streaking frequencies $n\omega$. For $n \leq 2$, the extracted ionization time aligns with Coulomb-free quantum-orbit predictions. At higher frequencies ($n \geq 3$), a distinct advancement of ionization times emerges. To elucidate this frequency-dependent shift, we compute probe-field-free Coulomb-modified ionization times using three distinct frameworks: (i) adiabatic correction (Appendix A), (ii) classical model (CM, Appendix B), and (iii) ARM method (Appendix C).[38,42,43]

Figures 4(b) and 4(c) display Coulomb-modified ionization times using different fundamental laser parameters. Obviously, excellent consistency emerges among the three theoretical frameworks [adiabatic correction estimated using Eq. (A13), CM, and ARM theory] with high-frequency TDSE-reconstructed ionization times. This finding underscores that selecting an appropriate streaking frequency is crucial to accurately measuring the Coulomb time shift. Moreover, the precision of the adiabatic correction [Eq. (A13)] supports a clear physical interpretation of the Coulomb-induced deceleration of the electron after ionization: after tunneling, the attractive Coulomb force opposes the electron's acceleration by the laser field. To overcome this decelerating influence and still return on time, the electron must tunnel earlier, allowing it to gain sufficient acceleration from the driving field.

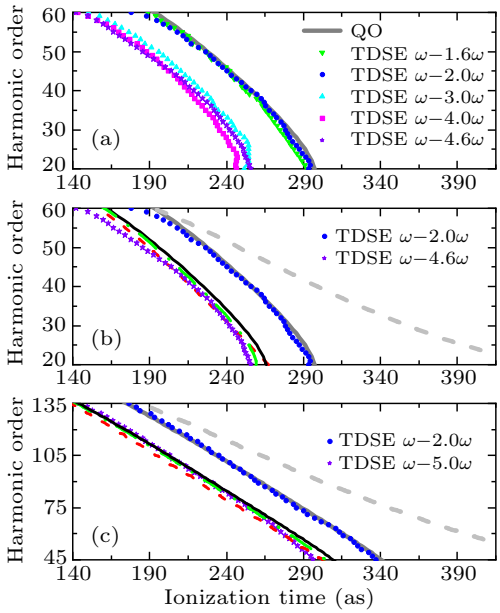


Fig. 4. (a) Ionization times reconstructed via TDSE simulations for 800 nm fundamental wavelength across multiple streaking-field frequencies. (b), (c) TDSE outcomes for distinct driving laser fields [(b) 800 nm and (c) 1200 nm], comparing reconstructed ionization times against theoretical predictions: adiabatic correction (black solid lines), trajectory-based classical model (red dashed lines), ARM (green dashed-dotted lines) and the simple man's model (light-gray thick lines). Gray traces across (a)–(c): real-valued ionization times from QO formalism. Laser intensities: 4.0×10^{14} W/cm^2 (a), (b) and 3.51×10^{14} W/cm^2 (c). Taken from Ref. [26].

To enhance physical understanding, we generalize CM and ARM theories to full orthogonal two-color fields. The objective is to establish approximate theoretical approaches that serve as alternatives to TDSE for extracting the optimal phase, from which the ionization time can be determined. In the CM, the optimal phase $\bar{\phi}$ ensures nullification of the transverse position at the recombination time t_r': $y(t_r') = 0$. Equation (7) satisfaction demands initial lateral velocity

$$\dot{y}(t_i^0) = \mathrm{Re}(A_y(t_i^0) - A_y(t_i)), \tag{13}$$

where $A_y(t)$ denotes the y-component of the vector potential $\boldsymbol{A}(t)$. For ARM, phase optimization maximizes harmonic intensity:

$$I_a = \left|\exp\left[\mathrm{i}\Omega t_r'' - \mathrm{i}S_v\left(t_i'', t_r''\right) - \mathrm{i}S_c\left(t_i'', t_r''\right)\right]\right|^2, \tag{14}$$

where saddle-point times t_i'', t_r'' are calculated under full OTC fields. Using CM/ARM-derived phases, ionization times can be extracted identically to TDSE procedures. Figure 5 presents the extracted ionization times in streaking frequencies $n\omega$ for harmonic orders $q = 43$ and $q = 53$. Although these results (CM, ARM, and TDSE) differ quantitatively, all reveal a dual-plateau structure transitioning progressively from low to high frequencies. The initial plateau corresponds precisely to Coulomb-free quantum-orbit predictions. This recalls orthogonal streaking measurements with a bicircular attoclock[44] (effective streaking threshold $\approx 2.1\omega$), where Coulomb time shifts are invisible. In contrast, the secondary plateau represents Coulomb-modified ionization times, confirming that Coulomb-induced shifts become accessible through appropriate tuning of the streaking frequency.

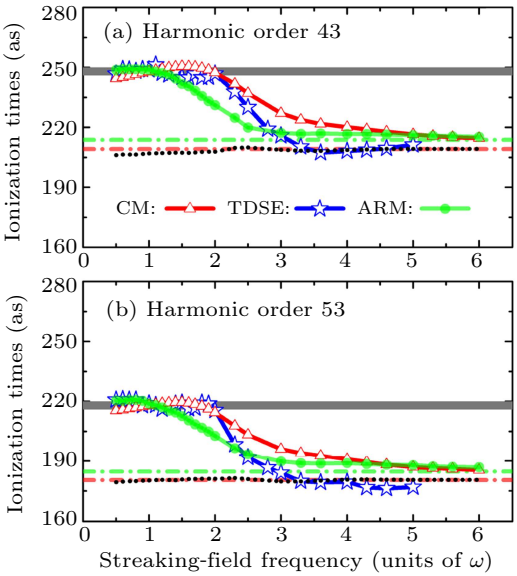


Fig. 5. Extracted ionization times versus streaking frequency for harmonic orders (a) 43 and (b) 53, generated using an 800 nm driving pulse. Horizontal benchmarks depict reference ionization times without streaking fields: QO model (gray solid lines), CM (red dashed-dotted lines), and ARM (green dashed-dotted lines). Black dotted curves: modified CM model predictions excluding lateral Coulomb forces. Taken from Ref. [26].

In the CM that neglects the Coulomb force along y, the reconstructed ionization times become nearly independent of the frequency of probe fields and match well with the second plateau of TDSE results (dotted curves, Fig. 5). This identifies probe-direction Coulomb interactions as the principal error source in low-frequency OTC techniques.

These findings are experimentally relevant because they suggest that the short-wavelength streaking field, such as 200 nm, is more effective for probing the Coulomb time shift with attosecond temporal resolution. To our knowledge, OTC HHG using an 800 nm–200 nm configuration, which would also generate even harmonics polarized along the y-axis like ω–2ω schemes, remains experimentally unexplored. Nevertheless, interest in unconventional probe wavelengths[45–47] confirms the feasibility of streaking across a range of wavelengths.

4. Coulomb-induced ionization time shift for long trajectories

Experimental advances successfully enable the separation of quantum trajectories, including the less studied long trajectory, which is crucial for trajectory-resolved high harmonic spectroscopy.[21,39,48–50] Its unique temporal detection range establishes significant potential for attosecond metrology.

The two observables for long trajectories, plotted as functions of harmonic orders and two-color phase delay, are shown in Fig. 6. An ω–2ω field is used with $\omega = 0.057$ a.u. and an intensity of 4.0×10^{14} W/cm^2. Both the harmonic intensity $I_G(\Omega, t_e)$ and the amplitude ratio R [Figs. 6(a) and 6(b)] vary with the two-color delay. The optimal phase ($\bar{\phi}_1$, $\bar{\phi}_2$) maximizing distinct observables exhibits opposite harmonic-order dependencies: $\bar{\phi}_1$ decreases marginally while $\bar{\phi}_2$ increases — directly inverting short-trajectory trends apparent in Fig. 3.

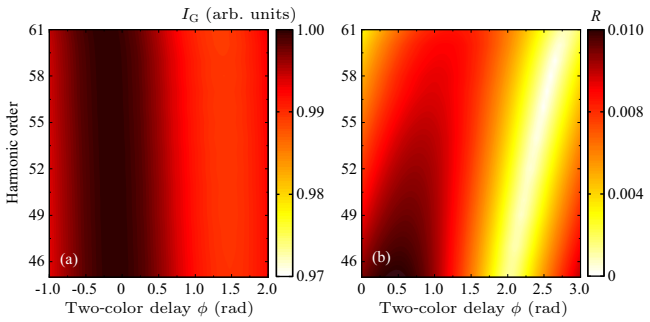


Fig. 6. TDSE-computed harmonic characteristics in ω–2ω fields. (a) Normalized spectral intensity and (b) y/x harmonic amplitude ratio versus harmonic order and two-color phase delay. Taken from Ref. [27].

For the TDSE results shown in Fig. 7, we implement the same approximations of the imaginary parts of (t_i, t_r) as the short trajectory case. The real components of (t_i, t_r) are then retrieved by inserting the measurable optimal phases ($\bar{\phi}_1$ and $\bar{\phi}_2$) into Eqs. (5)–(8). The long-trajectory TDSE data demonstrate excellent consistency with QO predictions, revealing

negligible Coulomb effects during ω–2ω measurement. Interestingly, return times exhibit significant deviations between the simple man's model and the QO approach, whereas ionization times maintain consistent values.

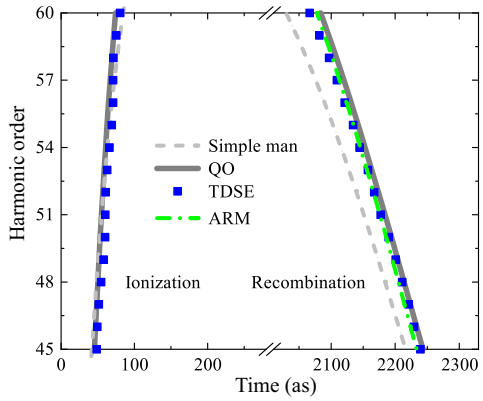


Fig. 7. Long-trajectory time parameters in HHG: ω–2ω scheme measurements derived from TDSE observables (squares) against theoretical predictions from QO (solid gray lines) and simple man's model (dashed gray lines). The ARM-calculated Coulomb-modified return time appears as green dashed-dotted line. Taken from Ref. [27].

Similarly to short-trajectory cases, we investigate the Coulomb effects on ionization time using three theoretical models: the adiabatic model, CM, and ARM. Figure 8 compares their computed ionization times against QO predictions. Among these approaches, we observe a $\sim$ 30-attosecond time shift, which is earlier than QO benchmarks. This echoes the short-trajectory behavior and questions the capacity of the OTC scheme to resolve such time shifts induced by the Coulomb potential.

Next, our OTC-based reconstruction utilizes harmonic intensity exclusively, i.e., implementing only displacement gates while excluding velocity gates. Recombination time parameters are constrained as follows: real components fixed to QO-predicted values with zero imaginary parts. This simplification is justified by our earlier results that the reconstructed recombination times in Fig. 7 closely match those of the QO model. For comparison, we also include the recombination time calculated using ARM theory (green lines in Fig. 7), which is also in line with the QO results.

Figure 8 compares TDSE-derived ionization times for two streaking configurations: low-frequency (2.6ω) and high-frequency (5ω) regimes. For the (ω–2.6ω) configuration, the QO-predicted (Coulomb-free) ionization times agree with the TDSE results. Whereas the ω–5ω configuration requires Coulomb-corrected times for optimal agreement. This demonstrates Coulomb effects becoming observable only in high-frequency streaking, enabling time shift retrieval. Furthermore, the remarkable consistency between classical (adiabatic/CM) and quantum (ARM) models indicates minimal under-barrier Coulomb influence. Consequently, Coulomb-induced shifts remain classically interpretable for both short- and long-trajectory cases.

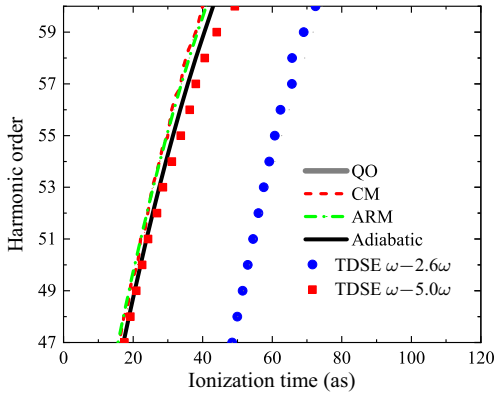


Fig. 8. Ionization times incorporating Coulomb effects: adiabatic approach (black solid lines), CM (red dashed lines), and ARM (green dashed-dotted lines). TDSE-based OTC results for $n = 2.6$ (low-frequency streaking) and $n = 5$ (high-frequency streaking) shown with QO reference (gray solid lines). Taken from Ref. [27].

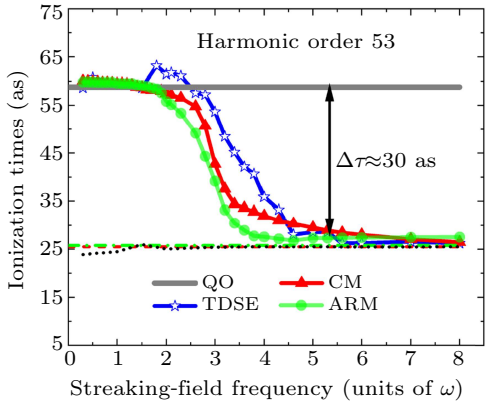


Fig. 9. Streaking-frequency-dependent ionization times ($q = 53$): TDSE (blue stars), CM (red triangles), and ARM (green circles). Horizontal references denote one-color models. The black dotted line shows two-color CM excluding the y-component Coulomb force. Taken from Ref. [27].

Our frequency-dependent time retrieval results for long trajectories closely resemble those for the short-trajectory case. In this context, both the classical model and the ARM theory have been extended to the OTC field configuration; details are provided in Section 3. Figure 9 presents the probed ionization times for order $q = 53$. These three approaches (TDSE, ARM, and CM) based on OTC fields exhibit a characteristic double-plateau structure. In the first plateau, the retrieved ionization times match those from the QO model, indicating that Coulomb interactions do not significantly affect the results. This observation is consistent with previous findings in photoelectron studies, where orthogonal streaking in an attoclock setup yielded ionization times largely unaffected by Coulomb effects.[44] When the streaking frequency equals the fundamental frequency ($n\omega = \omega$), all models produce $\bar{\phi}_1 \equiv 0\,(\mathrm{mod}\,\pi)$, since this configuration results in a linearly polarized total field. This prevents lateral displacement, and thus preserves harmonic yield. Indeed, at $n = 1$, the numerically optimized phases and the corresponding ionization times from all models are nearly identical and agree very well

with the quantum-orbit result. However, the secondary plateau reveals measurable Coulomb shifts, aligning with Coulomb-corrected single-color model predictions (horizontal lines in Fig. 9). Although the extent of plateaus differs slightly between the TDSE, CM, and ARM results, a good approximation is that the first plateau extends up to at least $n\omega = 2\omega$, while the second plateau begins before $n\omega = 5\omega$.

To investigate frequency-dependent disparities, we analyze a modified CM model that neglects Coulomb interactions along the y-axis (dotted lines in Fig. 9). Here, the probed ionization times become frequency-insensitive, matching the TDSE's secondary plateau. This indicates that the OTC retrieval method would yield accurate results in the absence of Coulomb forces in the probe's direction. Therefore, the failure of the low-frequency OTC method to retrieve the Coulomb time shift can be attributed to probe-direction Coulomb interactions, an effect not accounted for in the standard retrieval equations.

5. Summary and outlook

In summary, we have investigated the ionization-time shift induced by the electron–core interaction for both short and long trajectories in HHG. Our results show that the OTC probe scheme with high-frequency streaking (e.g., 5ω instead of 2ω) can accurately resolve the Coulomb-induced time shift.[26,27] This finding is supported by both classical trajectory models and quantum-mechanical theory. A key advantage of the high-frequency approach is that the retrieval formulas employed to probe the ionization times do not require explicit knowledge of the Coulomb interaction. However, this benefit comes at the cost of increased experimental complexity compared to the more commonly used ω–2ω scheme.

To address this issue, we introduce a Coulomb adjustment to electron dynamics within the two-color framework, yielding revised extraction equations for temporal information derivation from observables.[28,29] As shown in Ref. [29], the overall trend induced by the Coulomb correction remains intact: the modification shifts the TDSE-retrieved ionization times away from the QO model toward earlier times. However, the ionization times reconstructed from TDSE still show significant deviations from those predicted by the ARM and adiabatic models. Interestingly, the adiabatic model, involving the real Coulomb kick, predicts the right Coulomb time shift. Future work will be valuable in refining the retrieval method by incorporating Coulomb corrections beyond the static field approximation.[29,51] Furthermore, it is of great interest to identify additional experimental observables, such as varying the probe field frequency, and to continue developing advanced two-color field detection techniques. These efforts have the potential to reconstruct complete quantum trajectories, including information on electron tunneling dynamics, without prior knowledge of the real parts of the complex ionization and return times in HHG.[15,52]

Appendix A: Adiabatic correction

This appendix details the adiabatic framework implemented to assess Coulomb modifications to ionization and recombination times of electron trajectories in HHG. Calculations incorporate exclusively the linearly polarized driving field $E_x(t)$, defined as

$$E_x(t) = E_0\cos(\omega t) = -\partial A_x(t)/\partial t, \tag{A1}$$

where $A_x(t) = -E_0\sin(\omega t)/\omega$ represents the vector potential. Within this paradigm, electrons traverse classical trajectories between ionization (τ_i) and recombination (τ_r) events. The term 'adiabatic' specifies trajectory initialization via (1) tunnel-exit positioning determined through static-field approximation of a triangular potential and (2) initial velocity incorporating Coulomb-derived momentum shifts computed under static-field tunneling conditions.

Electron trajectories originate at $x_\mathrm{i} = -I_\mathrm{p}/E_x(\tau_\mathrm{i})$ (tunnel exit) and end at $x_\mathrm{r} = 0$, necessary for HHG re-collisional dynamics. Propagation neglects Coulomb forces, except for the initial velocity component. Consequently, the displacement between the ionization time and the return time follows

$$x_\mathrm{r} - x_\mathrm{i} = \int_{\tau_\mathrm{i}}^{\tau_\mathrm{r}} [p_x(\tau_\mathrm{i},\tau_\mathrm{r}) + A_x(t)]\,\mathrm{d}t, \tag{A2}$$

with canonical momentum $p_x(\tau_\mathrm{i},\tau_\mathrm{r})$ defined as

$$p_x(\tau_\mathrm{i},\tau_\mathrm{r}) = (x_\mathrm{r} - x_i)/(\tau_\mathrm{r} - \tau_\mathrm{i}) - \frac{1}{\tau_\mathrm{r} - \tau_\mathrm{i}}\int_{\tau_\mathrm{i}}^{\tau_\mathrm{r}} A_x(t)\mathrm{d}t. \tag{A3}$$

Using this, the velocities at τ_i and τ_r become

$$v_x(\tau_\mathrm{i}) = p_x(\tau_\mathrm{i},\tau_\mathrm{r}) + A_x(\tau_\mathrm{i}), \tag{A4}$$

$$v_x(\tau_\mathrm{r}) = p_x(\tau_\mathrm{i},\tau_\mathrm{r}) + A_x(\tau_\mathrm{r}). \tag{A5}$$

At the same time, the initial velocity that incorporates the adiabatic Coulomb shift along the x direction[53,54] is

$$v_x(\tau_\mathrm{i}) = \frac{\alpha\pi E_x(\tau_\mathrm{i})}{(2I_\mathrm{p})^{3/2}}, \tag{A6}$$

where the parameter α characterizes the Coulomb strength: $\alpha = 1$ signifies the full interaction while $\alpha = 0$ indicates the Coulomb-free case. For $\alpha = 0$, ionization/return times are denoted by τ_i^0 and τ_r^0. Harmonic generation at frequency Ω requires return velocity

$$v_x(\tau_\mathrm{r}) = \sqrt{2(\Omega - I_\mathrm{p})}, \tag{A7}$$

where the positive root is taken under the assumption that the electron returns from the negative side, implying a positive electric field at the ionization time, $E_x(\tau_\mathrm{i}) > 0$.

Applying the first-order Coulomb perturbation analysis to Eqs. (A4)–(A8), the ionization and recombination times exhibit shifts $\mathrm{d}\tau_\mathrm{i}$ and $\mathrm{d}\tau_\mathrm{r}$ governed by

$$\begin{aligned}\mathrm{d}v_x(\tau_\mathrm{i}) &= \alpha\frac{\pi E_x(\tau_\mathrm{i}^0)}{(2I_\mathrm{p})^{3/2}}\\ &= \left.\frac{\partial p_x}{\partial\tau_\mathrm{i}}\right|_{\tau_\mathrm{i}^0,\tau_\mathrm{r}^0}\mathrm{d}\tau_\mathrm{i} + \left.\frac{\partial p_x}{\partial\tau_\mathrm{r}}\right|_{\tau_\mathrm{i}^0,\tau_\mathrm{r}^0}\mathrm{d}\tau_\mathrm{r} + \left.\frac{\partial A_x(\tau_\mathrm{i})}{\partial\tau_\mathrm{i}}\right|_{\tau_\mathrm{i}^0}\mathrm{d}\tau_\mathrm{i}, \qquad \text{(A8)}\\ \mathrm{d}v_x(\tau_\mathrm{r}) &= 0\\ &= \left.\frac{\partial p_x}{\partial\tau_\mathrm{i}}\right|_{\tau_\mathrm{i}^0,\tau_\mathrm{r}^0}\mathrm{d}\tau_\mathrm{i} + \left.\frac{\partial p_x}{\partial\tau_\mathrm{r}}\right|_{\tau_\mathrm{i}^0,\tau_\mathrm{r}^0}\mathrm{d}\tau_\mathrm{r} + \left.\frac{\partial A_x(\tau_\mathrm{r})}{\partial\tau_\mathrm{r}}\right|_{\tau_\mathrm{r}^0}\mathrm{d}\tau_\mathrm{r}. \qquad \text{(A9)}\end{aligned}$$

Simultaneously solving Eqs. (A8) and (A9) yields Coulomb-modified time shifts

$$\begin{aligned}\mathrm{d}\tau_\mathrm{i} =& -\frac{\alpha\pi}{(2I_\mathrm{p})^{3/2}}\\ &\times\frac{\left(\tau_\mathrm{r}^0-\tau_\mathrm{i}^0\right)E_x(\tau_\mathrm{r}^0)+v_\mathrm{r}}{\left(\tau_\mathrm{r}^0-\tau_\mathrm{i}^0\right)E_x(\tau_\mathrm{r}^0)+v_\mathrm{r}+\frac{I_\mathrm{p}\dot{E}_x(\tau_\mathrm{i}^0)E_x(\tau_\mathrm{r}^0)}{E_x^3(\tau_\mathrm{i}^0)}}, \qquad \text{(A10)}\\ \mathrm{d}\tau_\mathrm{r} =& \frac{\alpha\pi}{(2I_\mathrm{p})^{3/2}}\\ &\times\frac{I_\mathrm{p}\dot{E}_x(\tau_\mathrm{i}^0)/E_x^2(\tau_\mathrm{i}^0)}{(\tau_\mathrm{r}^0-\tau_\mathrm{i}^0)E_x(\tau_\mathrm{r}^0)+v_\mathrm{r}+\frac{I_\mathrm{p}\dot{E}_x(\tau_\mathrm{i}^0)E_x(\tau_\mathrm{r}^0)}{E_x^3(\tau_\mathrm{i}^0)}}. \qquad \text{(A11)}\end{aligned}$$

Here, the electric-field time-derivative terms originate from

$$\left.\frac{\partial x_\mathrm{i}}{\partial\tau_\mathrm{i}}\right|\tau_\mathrm{i}^0 = I_\mathrm{p}\dot{E}x(\tau_\mathrm{i}^0)/E_x^2(\tau_\mathrm{i}^0). \qquad \text{(A12)}$$

If the tunnel exit position is assumed to be independent of the ionization time, i.e., $\left.\frac{\partial x_\mathrm{i}}{\partial\tau_\mathrm{i}}\right|\tau_\mathrm{i}^0 = 0$, the ionization time shift simplifies to the adiabatic correction

$$\mathrm{d}\tau_\mathrm{i} = -\alpha\pi/\left(2I_\mathrm{p}\right)^{3/2}, \qquad \text{(A13)}$$

while the return time shift $\mathrm{d}\tau_\mathrm{r}$ vanishes, as reported in Ref. [26]. Compared to this simplified correction, Eq. (A10) predicts an additional small advance of the ionization time, with the difference depending weakly on the harmonic order and ranging from approximately 2–7 as.

The final Coulomb-modified time information for this adiabatic correction is calculated by adding $\mathrm{d}\tau_\mathrm{i}$ and $\mathrm{d}\tau_\mathrm{r}$ to the corresponding Coulomb-free values provided by the QO model.

Appendix B: Classical model

In this model, the electron trajectory $\boldsymbol{r}(t)$ evolves according to Newton's equation

$$\ddot{\boldsymbol{r}}(t) = -\boldsymbol{E}(t) - \nabla_{\boldsymbol{r}}V\left(\boldsymbol{r}(t)\right), \qquad \text{(B1)}$$

where the Coulomb potential $V(\boldsymbol{r})$ — identical to that in the TDSE — is incorporated non-perturbatively after tunneling processes. The initial conditions are set as

$$\dot{\boldsymbol{r}}(t_\mathrm{i}^0) = \mathrm{Re}\left[\boldsymbol{p}(t_\mathrm{i},t_\mathrm{r}) + \boldsymbol{A}(t_\mathrm{i}^0)\right], \qquad \text{(B2)}$$

$$\boldsymbol{r}(t_\mathrm{i}^0) = \mathrm{Re}\left(\int_{t_\mathrm{i}}^{t_\mathrm{i}^0}\left[\boldsymbol{p}(t_\mathrm{i},t_\mathrm{r}) + \boldsymbol{A}(t)\right]\mathrm{d}t\right), \qquad \text{(B3)}$$

aligned with the QO approach that neglects Coulomb effects during tunneling.

Recombination occurs at t_r' when $\boldsymbol{r}(t_\mathrm{r}') = 0$, indicating the recollision of electrons and parent ions. At this instant, the electron's return energy E_r determines the energy of emitted photons:

$$\Omega'\left(t_\mathrm{i}^0,t_\mathrm{r}'\right) = I_\mathrm{p} + E_\mathrm{r} = I_\mathrm{p} + \frac{\dot{\boldsymbol{r}}^2(t_\mathrm{r}')}{2} + V\left(\boldsymbol{r}(t_\mathrm{r}')\right), \qquad \text{(B4)}$$

with E_r accounting for both kinetic and potential contributions. The primed notation (t_r', Ω') distinguishes these from the QO-model counterparts used in initialization.

The ionization times corresponding to a given harmonic order q are obtained via establishing the mapping between Ω' and t_i^0. Benchmark testing confirms close agreement between CM times (τ_i, τ_r) and the real components of complex QO times in Coulomb-free simulations.

Appendix C: Analytical R-matrix method

We follow the theoretical framework developed in Refs. [38,42], where the first-order corrections are introduced to the QO model accounting for electron–core interactions. For completeness, the relevant equations are summarized below. A similar approach has also been reported in Ref. [55]. Within ARM theory, electron–core dynamics employ the Coulomb potential $U(\boldsymbol{r}) = -1/|\boldsymbol{r}|$. The resulting Coulomb phase, quantifying the influence of core-interaction on the time parameters of electronic trajectories in HHG, is given by

$$S_\mathrm{c} = \int_{t_k}^{t_\mathrm{end}}\mathrm{d}t\; U\left(\boldsymbol{r}_\mathrm{a}(t)\right), \qquad \text{(C1)}$$

which supplements the standard semiclassical action S_v (Eq. 10). The classical trajectory in the integrand corresponds to the Coulomb-free path,

$$\boldsymbol{r}_\mathrm{a}(t) = \int_{t_\mathrm{i}}^{t}\left(\boldsymbol{p}(t_\mathrm{i},t_\mathrm{r}) + \boldsymbol{A}\left(t'\right)\right)\mathrm{d}t'. \qquad \text{(C2)}$$

The lower integration limit t_k is dictated via a boundary matching condition that separates the configuration space into inner and outer regions, divided by a spherical boundary. This matching prevents the trajectory from approaching the ionic core too closely within the Coulomb potential, as discussed in Ref. [42]. Explicitly, $t_k = t_\mathrm{i} - i/\left(2I_\mathrm{p}\right)$. The upper integration limit t_end corresponds to the time when the electron returns to the position

$$r_0 = \frac{\exp\left[2\left(0.5772 - \sum_{l=1}^{\infty}\left[1 - v_\mathrm{r}t\arctan\left(1/\left(v_\mathrm{r}t\right)\right)\right]/l\right)\right]}{2v_\mathrm{r}}, \qquad \text{(C3)}$$

with the recombination velocity of electrons defined as $v_r = \sqrt{2\left(q\omega - I_p\right)}$.[38,43] Using this framework, first-order corrections to the real parts of the saddle-point times are obtained as[38]

$$\Delta t_i^0 = -\frac{\partial\,\mathrm{Re}\,S_c}{\partial I_p} - \frac{\partial\,\mathrm{Re}\,S_c}{\partial \Omega}, \quad \Delta t_r^0 = -\frac{\partial\,\mathrm{Re}\,S_c}{\partial \Omega}. \tag{C4}$$

These derivatives are computationally evaluated through finite differences of the Coulomb phase with respect to I_p and Ω.

Acknowledgements

The authors appreciate the expert guidance and continuous support of Prof. Manfred Lein (Leibniz University Hannover, Institute of Theoretical Physics), under whose supervision the main results summarized in this review were obtained. They also acknowledge funding from the National Natural Science Foundation of China (Grant Nos. 12204209 and 12274188), Natural Science Foundation of Gansu Province (Grant No. 23JRRA1090), Fundamental Research Funds for Central Universities (Grant No. lzujbky-2023-ey08), and Cultivation Project for Outstanding Young Teachers in Anhui Provincial Universities (Grant No. YQYB2025099).

References

[1] Andreas V, Di W, Adrian J, Belen M, Christopher B, Chinmaya J, Everett L, Moungi B, Diega G and Ramesh R 2013 *ACM Trans. Graphics* **32** 44
[2] Cocker T L, Peller D, Yu P, Repp J and Huber R 2016 *Nature* **539** 263
[3] Peplow M 2017 *Nature* **544** 408
[4] Roelcke C, Kastner L Z, Graml M, Biereder A, Wilhelm J, Repp J, Huber R and Gerasimenko Y A 2024 *Nat. Photon.* **18** 595
[5] Corkum P B and Krausz F 2007 *Nat. Phys.* **3** 381
[6] McPherson A, Gibson G, Jara H, Johann U, Luk T S, McIntyre I A, Boyer K and Rhodes C K 1987 *J. Opt. Soc. Am. B* **4** 595
[7] Ferray M, L'Huillier A, Li X F, Lompre L A, Mainfray G and Manus C 1988 *J. Phys. B: At. Mol. Opt. Phys.* **21** L31
[8] Blaga C I, Catoire F, Colosimo P, Paulus G G, Muller H G, Agostini P and DiMauro L F 2009 *Nat. Phys.* **5** 335
[9] Camus N, Yakaboylu E, Fechner L, Klaiber M, Laux M, Mi Y, Hatsagortsyan K Z, Pfeifer T, Keitel C H and Moshammer R 2017 *Phys. Rev. Lett.* **119** 023201
[10] Li W, Fan X, Pan S, Wenkai T, Xu S, Jiacan W, Zhigang Z, Jing Z, Xiaowei W and Zengxiu Z 2023 *Chin. Phys. Lett.* **40** 114203
[11] Yongzhe M, Hongcheng N and Jian W 2024 *Chin. Phys. B* **33** 013201
[12] Corkum P B 1993 *Phys. Rev. Lett.* **71** 1994
[13] Lewenstein M, Balcou P, Ivanov M Y, L'Huillier A and Corkum P B 1994 *Phys. Rev. A* **49** 2117
[14] Salières P, Carré B, Déroff L L, Grasbon F, Paulus G G, Walther H, Kopold R, Becker W, Milošević D B, Sanpera A and Lewenstein M 2001 *Science* **292** 902
[15] Kneller O, Azoury D, Federman Y, Krüger M, Uzan A J, Orenstein G, Bruner B D, Smirnova O, Patchkovskii S, Ivanov M and Dudovich N 2022 *Nat. Photon.* **16** 304
[16] Babushkin I, Galán Á J, de Andrade J R C, Husakou A, Morales F, Kretschmar M, Nagy T, Vaičaitis V, Shi L, Zuber D, Bergé L, Skupin S, Nikolaeva I A, Panov N A, Shipilo D E, Kosareva O G, Pfeiffer A N, Demircan A, Vrakking M J J, Morgner U and Ivanov M 2022 *Nat. Phys.* **18** 417
[17] Leeuwenburgh J, Cooper B, Averbukh V, Marangos J P and Ivanov M 2013 *Phys. Rev. Lett.* **111** 123002
[18] Cooper B and Averbukh V 2013 *Phys. Rev. Lett.* **111** 083004
[19] Lein M 2005 *Phys. Rev. Lett.* **94** 053004
[20] Baker S, Robinson J S, Haworth C, Teng H, Smith R, Chirilă C C, Lein M, Tisch J and Marangos J P 2006 *Science* **312** 424
[21] Lan P, Ruhmann M, He L, Zhai C, Wang F, Zhu X, Zhang Q, Zhou Y, Li M, Lein M and Lu P 2017 *Phys. Rev. Lett.* **119** 033201
[22] Lakhotia H, Kim H Y, Zhan M, Hu S, Meng S and Goulielmakis E 2020 *Nature* **583** 55
[23] Dudovich N, Smirnova O, Levesque J, Mairesse Y, Ivanov M Y, Villeneuve D M and Corkum P B 2006 *Nat. Phys.* **2** 781
[24] Shafir D, Soifer H, Bruner B D, Dagan M, Mairesse Y, Patchkovskii S, Ivanov M Y, Smirnova O and Dudovich N 2012 *Nature* **485** 343
[25] Zhao J and Lein M 2013 *Phys. Rev. Lett.* **111** 043901
[26] Yue S, Xue S, Du H and Lein M 2022 *Phys. Rev. A* **105** L041103
[27] Yue S, Li Y, Xue S, Du H and Lein M 2022 *Phys. Rev. A* **106** 023117
[28] Yue S, Liu J, Xue S, Du H and Lein M 2023 *Phys. Rev. A* **107** 063102
[29] Yue S, Liu J, Xue S, Du H and Lein M 2025 *Phys. Rev. A* **111** 039902
[30] Crank J and Nicolson P 1947 *Proc. Cambridge Philos. Soc.* **43** 50
[31] Nurhuda M and Faisal F H M 1999 *Phys. Rev. A* **60** 3125
[32] Ehrenfest P 1927 *Zeitschrift für Physik* **45** 455
[33] Chirilă C C, Dreissigacker I, van der Zwan E V and Lein M 2010 *Phys. Rev. A* **81** 033412
[34] Yue S, Brennecke S, Du H and Lein M 2020 *Phys. Rev. A* **101** 053438
[35] Krausz F and Ivanov M 2009 *Rev. Mod. Phys.* **81** 163
[36] Ivanov M Y, Spanner M and Smirnova O 2005 *J. Mod. Opt.* **52** 165
[37] Shafir D, Mairesse Y, Villeneuve D M, Corkum P B and Dudovich N 2009 *Nat. Phys.* **5** 412
[38] Torlina L and Smirnova O 2017 *New J. Phys.* **19** 023012
[39] Le A T, Lucchese R R, Lee M T and Lin C D 2009 *Phys. Rev. Lett.* **102** 203001
[40] van der Zwan E V and Lein M 2012 *Phys. Rev. Lett.* **108** 043004
[41] Keldysh L V 1965 *Sov. Phys. JETP* **20** 1307
[42] Torlina L and Smirnova O 2012 *Phys. Rev. A* **86** 043408
[43] Ivanov M and Smirnova O 2011 *Phys. Rev. Lett.* **107** 213605
[44] Eicke N, Brennecke S and Lein M 2020 *Phys. Rev. Lett.* **124** 043202
[45] Watanabe S, Kondo K, Nabekawa Y, Sagisaka A and Kobayashi Y 1994 *Phys. Rev. Lett.* **73** 2692
[46] Kroh T, Jin C, Krogen P, Keathley P D, Calendron A L, Siqueira J P, Liang H K, Falcão-Filho E L, Lin C D, Kärtner F X and Hong K H 2018 *Opt. Express* **26** 16955
[47] Mitra S, Biswas S, Schötz J, Pisanty E, Förg B, Kavuri G A, Burger C, Okell W, Högner M, Pupeza I, Pervak V, Lewenstein M, Wnuk P and Kling M F 2020 *J. Phys. B* **53** 134004
[48] Dudovich N, Smirnova O, Levesque J, Mairesse Y, Ivanov M Y, Villeneuve D and Corkum P B 2006 *Nat. Phys.* **2** 781
[49] Brugnera L, Hoffmann D J, Siegel T, Frank F, Zaïr A, Tisch J W G and Marangos J P 2011 *Phys. Rev. Lett.* **107** 153902
[50] Camper A, Ferré A, Blanchet V, Descamps D, Lin N, Petit S, Lucchese R, Salières P, Ruchon T and Mairesse Y 2023 *Phys. Rev. Lett.* **130** 083201
[51] Qiao S, Li L, Cui H, Zeng S, Liang S, Lan P and Lu P 2025 *Phys. Rev. A* **111** 053114
[52] Pedatzur O, Orenstein G, Serbinenko V, Soifer H, Bruner B D, Uzan A J, Brambila D S, Harvey A G, Torlina L, Morales F, Smirnova O and Dudovich N 2015 *Nat. Phys.* **11** 815
[53] Shvetsov-Shilovski N I, Goreslavski S P, Popruzhenko S V and Becker W 2009 *Laser Phys.* **19** 1550
[54] Goreslavski S P, Paulus G G, Popruzhenko S V and Shvetsov-Shilovski N I 2004 *Phys. Rev. Lett.* **93** 233002
[55] Popruzhenko S V 2018 *J. Phys. B: At. Mol. Opt. Phys.* **51** 144006